Aerospace Science and Technology 158 (2025) 109883

Contents lists available at ScienceDirect

Aerospace Science and Technology

journal homepage: www.elsevier.com/locate/aescte

Impact of installation on the performance of a civil turbofan exhaust at wind-milling: A combined experimental and numerical approach

Ioannis Goulos [a], David MacManus [a], Josep Hueso Rebassa [a], James Alderman [b], Christopher Sheaf [c]

[a] Centre for Propulsion and Thermal Power Engineering, School of Aerospace, Transport, and Manufacturing, Cranfield University, MK43 0AL, UK
[b] Aircraft Research Association Ltd, Manton Lane, Bedford, MK41 7PF, UK
[c] Installation Aerodynamics, Rolls-Royce plc, Moor Lane D3, Derby, DE24 8BJ UK

ARTICLE INFO

Communicated by Kontis Konstantinos

Keywords:
Aerospace
Turbofan
Aerodynamics
Computational fluid dynamics
Installation propulsion
Integration
Wind-milling
Exhaust

ABSTRACT

This work presents a combined experimental and numerical investigation of the effect of wing integration on the aerodynamic behaviour of a typical large civil aero-engine exhaust at wind-milling conditions. Engine performance simulations established estimates of Fan and Core Nozzle Pressure Ratios ($FNPR$ and $CNPR$, respectively) for representative "engine-out" wind-milling scenarios. The experimental data and Reynolds Averaged Navier Stokes (RANS) Computational Fluid Dynamic (CFD) simulations encompassed End of Runway (EoR) take-off, diversion, and cruise wind-milling conditions for both isolated and installed configurations. The impact of $FNPR$, $CNPR$, free-stream Mach number (M_∞), and high-lift surfaces on the installed suppression effect were evaluated. The measured and CFD predicted fan and core nozzle maps were implemented into the engine performance model to estimate the engine re-matching characteristics due to the impact of the installation, and the effect on engine mass flow. The effect of installation can reduce the fan and core nozzle discharge coefficients by up to 13% and 26%, respectively, relative to the isolated configuration for representative EOR wind-milling conditions. RANS CFD captures the effect of suppression on both the fan and core with an accuracy between 0.1% and 1.2%, depending on Mach number, which is sufficient for industrial design and analysis purposes. The engine performance analyses showed that the installed suppression effect can result in a 10% reduction of engine mass flow at EOR wind-milling. Within the context of nacelle design under wind-milling, this effect of exhaust suppression must be considered in determining the intake Mass Flow Capture Ratio ($MFCR$).

1. Introduction

1.1. Background

Current trends in civil aviation tend towards an increase in propulsive efficiency by reducing specific thrust [1,2]. This is achieved through larger By-Pass Ratios (BPR) which are typically facilitated with larger fan diameters [3]. This trend is likely to be enabled with the use of compact nacelles to reduce the associated nacelle drag and weight penalties [4–6]. However, this increase in nacelle compactness may lead to a greater sensitivity of nacelle drag to the Mass Flow Capture Ratio (MFCR) at Off-Design (OD) conditions such as wind-milling [7,8]. The engine mass flow is dependent on the aerodynamic behaviour of the exhaust, and specifically on the fan nozzle discharge coefficient (C_d^{Fan}) [9].

During wind-milling the engine BPR is very high with most of the mass flow going through the bypass duct, and minimal flow passing through the core [10,11]. The fan nozzle operates unchoked with very low total to static pressure ratios [10,11]. This renders the mass flow discharged through the fan nozzle highly sensitive to the external static pressure field [12]. As a result, C_d^{Fan} can be sensitive to the effect of the pressure field produced by the airframe in-flight [13]. This effect can be further amplified by the presence of the high-lift surfaces [14,15]. This "installed pressure field", can suppress the fan nozzle mass flow leading to a reduction in engine ingested mass flow [13]. Hence, it is essential to understand the impact of this "installed pressure field" on the aerodynamic behaviour of the exhaust during wind-milling since it affects the engine ingested mass flow and the associated nacelle aerodynamics and drag [16].

E-mail address: i.goulos@cranfield.ac.uk (I. Goulos).

https://doi.org/10.1016/j.ast.2024.109883
Received 25 March 2024; Received in revised form 12 December 2024; Accepted 15 December 2024

Available online 17 December 2024
1270-9638/© 2025 Rolls-Royce Plc. Published by Elsevier Masson S.A.S. This is an open access article under the CC BY license (http://creativecommons.org/licenses/by/4.0/).

Nomenclature

Roman Symbols

$\dot{m}$	Mass flow rate, kg/sec
A	Surface area, m^2
C_d, C_v	Exhaust nozzle discharge and velocity coefficient
C_p^{mod}	Normalised static pressure coefficient
C_{ref}	Reference chord length, m
D_{Nozzle}^{Fan}	Fan nozzle exit diameter, m
k	Turbulent kinetic energy, m^2/sec^2
M and Re	Mach and Reynolds number
M_{is}	Isentropic Mach number
p and T	Static pressure (Pa) and temperature (K)
P_0, T_0	Stagnation pressure (Pa) and temperature (K)
R	Air gas constant, $J/(kg \times K)$
Tu_{in}	Turbulence intensity
y^+	Non-dimensional wall distance

Greek Symbols

γ	Specific heat capacity ratio
κ	Thermal conductivity, $J/(m \times K \times sec)$
λ	Total to ambient static nozzle pressure ratio
μ	Mean value
ω	Specific dissipation rate, $1/sec$
ρ	Flow density, kg/m^3
σ	Standard deviation

Superscripts

$Core$	Referring to the core nozzle
$Engine$	Referring to the engine
Fan	Referring to the fan nozzle

Subscripts

∞	Referring to ambient free-stream conditions
CFD	Referring to CFD flow solutions
$Crit.$	Referring to critical flow conditions
$Ideal$	Referring to ideal flow conditions
$Installed$	Referring to the installed configuration
$Isolated$	Referring to the isolated configuration
$Throat$	Referring to the nozzle throat

Acronyms

$AIAA$	American Institute of Aeronautics and Astronautics
ARA, TWT	Aircraft Research Association and Transonic Wind Tunnel
BC, BPR	Boundary Condition and By-Pass Ratio
$CNPR$	Core Nozzle Pressure Ratio, $= P_0^{Core}/p_\infty$
DP, OD	Design-Point and Off-Design, respectively
$DSFRN$	Dual Separate Flow Reference Nozzle
$DSJP$	Dual Stream Jet Propulsion
DTC	Digital Thermal Compensation
EOR	End Of Runway
ER	Extraction Ratio, $FNPR/CNPR$
$FNPR$	Fan Nozzle Pressure Ratio, $= P_0^{Fan}/p_\infty$
$HBR, VHBR$	High and Very High By-pass Ratio
LP	Low Pressure
LP, PS, SS	Low Pressure, Pressure Side, and Suction Side
RMS, $RMSD$	Root Mean Square (Deviation)

1.2. Exhaust performance metrics

The aerodynamic performance of the fan and core nozzles is typically quantified using the discharge and velocity coefficients, C_d and C_v, respectively [17,18]. The discharge coefficient C_d is defined as ratio of the actual nozzle mass flow to the ideal nozzle mass flow based on isentropic flow expansion to ambient static pressure. C_d accounts for internal losses within the nozzle as well as suppression effects [12,13]. Moreover, C_d accounts for changes to the exit static pressure to which the nozzle exhausts and can affect the nozzle mass flow. For typical civil aero-engine cases, these external static pressure changes relative to the ambient conditions can "suppress" the nozzle mass flow. These "suppression effects" are classified in three categories: (a)"Free-stream suppression" which stems from the impact of free-stream flow [19,20], (b) "Installed suppression" due to aerodynamics interactions between the engine and the airframe [17,21,22], and (c) "fan suppression" which is only pertinent for the core nozzle and is due to the impact of the fan nozzle flow on the core stream [19,20].

The velocity coefficient C_v is defined as the ratio of the actual nozzle gross thrust over the ideal nozzle gross thrust which would result from the actual nozzle mass flow under isentropic expansion. C_v quantifies the magnitude of the entropic effects within the nozzle and jet. These typically include skin friction and boundary layer growth within the duct, nozzle, pylon, and after-body, as well as shear layers, shock waves, and expansion fans within the jet [12].

1.3. Impact of installation on exhaust performance

The existing literature contains many references where the impact of installation on the aerodynamic behaviour of separate-jet exhausts has been investigated. Oliveira et al. [23] investigated numerically the mechanisms that govern the airframe-engine aerodynamic interference for a narrow-body twin-engine aircraft with a podded under-wing engine installation. It was shown that the formation of a "gully" flow between the wing, pylon, and the core after-body led to increased flow acceleration on the engine inboard side which amplified shock-losses. However, the impact of airframe-engine aerodynamic interference on exhaust performance in terms of C_d and C_v was not quantified. Furthermore, Oliveira et al. [23] focused solely at Design Point (DP) mid-cruise conditions.

Otter et al. [22] performed a RANS CFD investigation to evaluate the impact of installation on the aerodynamic behaviour of two aero-engines across a range of installation positions. Analyses were carried out for two aero-engine architectures with BPR of 11 and 18, respectively, at mid-cruise. Both engines were installed on the NASA Common Research Model (CRM) [24] in a podded under-wing configuration. The fan nozzle was unaffected by the installation effect because it was choked for both engines. However, a variation of $\approx 10\%$ was found for C_d^{Core} across the range of positions. This was because the core nozzle was unchoked and therefore it was more sensitive to installed suppression [22]. The work of Otter et al. [22] was similarly limited to mid-cruise conditions.

Goulos et al. [12] carried out a numerical investigation to quantify the impact of installation for a VHBR aero-engine at DP mid-cruise with $BPR \approx 15$ installed on the NASA CRM [24]. The work included close coupled installation positions, as well as the pylon. It was shown that due to the wing sweep and the nature of the aerodynamic interference mechanisms, the installation results in a notable lateral flow asymmetry on the exhaust at mid-cruise conditions. Goulos et al. [12] similarly noted that C_d^{Fan} was insensitive to changes in installation position because the fan nozzle was choked. However, a variation of 5% was found for the unchoked core nozzle C_d^{Core}. Close coupled positions exhibited higher values of C_d^{Core} compared to forward engine locations. The impact of installation at OD conditions was not assessed by Goulos et al. [12].

Rao et al. [13] quantified the impact of installation on the exhaust of an aero-engine operating at OD idle-descent conditions. Rao et al. [13]

found that C_d^{Fan} is reduced by about 1.6% across the idle-descent phase. The impact on C_d^{Core} was found to be more significant. C_d^{Core} increased by 43% at the top of descent, relative to the isolated configuration. However, at the end of descent, C_d^{Core} reduced by roughly 5.4%. This was due to a combination of parameters such as wing loading, Fan Nozzle Pressure Ratio (FNPR), and Core Nozzle Pressure Ratio (CNPR) which affected the core nozzle base pressure [13]. However, Rao et al. [13] did not present any CFD validation with experimental data for these OD conditions. Furthermore, Rao et al. [13] did not address the wind-milling flow regime where FNPR and CNPR are reduced compared to idle-descent.

Gomariz-Sancha et al. [25] developed a Dual-Stream Jet Propulsion (DSJP) rig for the testing of separate jet exhausts in isolated and installed configurations. The rig was equipped with the AIAA Dual Separate Flow Reference Nozzle (DSFRN) [26,19] installed under a swept wing. Tests were carried out in the Transonic Wind Tunnel (TWT) [27] at the Aircraft Research Association (ARA). Gomariz-Sancha et al. [25] measured C_d^{Fan} for $FNPR \in [1.4, 2.8]$ and for $M_\infty \in [0.2, 0.85]$. It was found that the impact of wing installation on C_d^{Fan} is negligible when the fan nozzle is choked. However, the wing installation has a detrimental effect on C_d^{Fan} for unchoked flow and this effect is amplified with decreasing FNPR. Specifically, the reduction in C_d^{Fan} due to the impact of wing installation was $\approx 1\%$ for $FNPR = 1.4$ and $M_\infty = 0.35$, when the 20-degree flap wing was deployed. Gomariz-Sancha et al. [25] quantified the impact of installation down to a minimum FNPR of 1.4. However, they did not investigate the wind-milling flow regime where FNPR can reduce down to ≈ 1.02, where the impact of installation is expected to increase [28].

Goulos et al. [28] investigated numerically the effect of wing integration on the aerodynamic behaviour of a typical civil large aero-engine exhaust at OD wind-milling conditions. The work was based on the DSJP configuration [25] at representative EOR, diversion, and cruise wind-milling conditions. It was shown that the installed pressure field can reduce C_d^{Fan} and C_d^{Core} by up to 16% and 13%, respectively, relative to the isolated configuration for representative EOR wind-milling conditions ($M_\infty = 0.3$, $FNPR = 1.03$, $CNPR = 1.03$). The installed flow suppression was laterally biased towards the fan cowl inboard side topline which was attributed to the proximity of the swept wing TE flap to the fan nozzle exit. The results of Goulos et al. [28] were used to inform the design and set-up of the experimental activity.

1.4. Scope of present work

The existing literature is predominantly focused on mid-cruise conditions [23,22,12,29], with the exception of the work of Rao et al. [13] and Goulos et al. [28] who investigated the idle-descent and wind-milling phases, respectively. For wind-milling conditions, recent studies focused on nacelle drag [16], internal drag [9], and fan stage aerodynamics [30–33]. Goulos et al. [28] were the first to quantify the installed suppression effect on separate-jet exhaust performance at wind-milling. However, the work did not include any validation based on experimental data. To the authors' knowledge there is no published study where the impact of installed suppression has been measured for wind-milling conditions. As a result, the accuracy of RANS CFD for exhaust performance prediction down to these sub-idle conditions is currently unknown. Furthermore, the impact of the installed pressure field on the engine air mass-flow during wind-milling has not been previously investigated. The installed pressure field can affect the engine re-matching and the internal system losses [9] with a reciprocal impact on the engine airflow. This change in MFCR can affect nacelle drag for the critical EOR, diversion, and cruise wind-milling conditions [7,8,16].

This article continues the work of Goulos et al. [28] by conducting a combined experimental and numerical investigation to quantify the impact of installed suppression on the aerodynamic performance of a civil High By-pass Ratio (HBR) aero-engine exhaust at wind-milling. The work used the DSJP rig [25], which was tested in the TWT [27] at the ARA. The experimental data and CFD simulations [34] encompassed End of Runway (EoR) take-off, diversion, and cruise wind-milling conditions for both isolated and installed configurations. The impact of $FNPR$, $CNPR$, free-stream Mach number (M_∞), and high-lift surfaces on the installed suppression effect were evaluated. Finally, the measured and predicted C_d^{fan} and C_d^{Core} maps were implemented into an engine performance model [35] to estimate the engine re-matching effect due to the impact of installation, and the reciprocal effect on engine mass flow and $MFCR$ which is a key parameter that affects nacelle drag under wind-milling conditions [36].

The novelty of the work is that this the first investigation to quantify experimentally and numerically the impact of installation on exhaust performance at wind-milling. The main contribution is that for the first time RANS CFD is validated for wind-milling exhaust performance and it is demonstrated that it can be used with confidence in an industrial design setting. These aspects have not been previously reported in the existing literature. Therefore, this work is the first of its kind to quantify the aerodynamic performance of civil aero-engine exhausts at the previously unexplored and challenging wind-milling flow regime. The work is complementary to sub-idle engine performance modelling methods as it is the first to introduce installed fan and core nozzle suppression maps that can be used to enhance wind-milling engine airflow predictions.

2. Methodology

2.1. ARA dual stream jet propulsion (DSJP) rig

The installed nozzle suppression tests and computational analyses were based on the DSJP rig (Fig. 1) [25] which was tested in the ARA TWT (Fig. 1(a)) [27]. The DSJP rig was designed to measure the installed suppression effect on the aerodynamic performance of a civil large aero-engine exhaust. The rig uses the AIAA DSFRN (Fig. 1(b)) [26,19], installed under a swept wing designed to emulate the lift-distribution of the NASA CRM wing [24] at the engine station.

Computational analyses were carried out for both isolated (Fig. 2(a)) and installed configurations (Fig. 2(b) and (c)) to quantify the impact of the wing on the fan and core nozzle discharge coefficients, C_d^{Fan} and C_d^{Core}, respectively. The impact of FNPR and CNPR, as well as free-stream M_∞ and high-lift surfaces on the installed suppression effect were also evaluated. To understand the impact of the high-lift surfaces two different wing configurations were analysed: (1) 0-degree flap wing (Fig. 2(b)) and (2) 20-degree flap wing (Fig. 2(c)). The former arrangement is representative of a clean-wing configuration for diversion and cruise. The latter configuration employs a 20-degree trailing edge flap that represents the high-lift surfaces for EOR-type configurations.

2.2. Experimental approach

The main internal features of the ARA DSJP rig [25] are shown in Fig. 3. The core and bypass flows are fed from 10 and 250 bar high-pressure systems, respectively [27]. Both air feeds enter via the strut into a fan and core plenum. The core and fan flows encounter a perforated plate which provides a homogeneous flow distribution and a pressure drop via an array of choked holes. The fan and core flows are further conditioned through a long cell honeycomb leading to the total temperature rakes. There are twin gauze flow conditioners before the fan and core P_0 rakes. Finally the flow exits through the core and fan nozzles.

Calculation of the fan and core discharge coefficients, C_d^{Fan} and C_d^{Core}, respectively, requires knowledge of the "real" and "ideal" nozzle mass flows [26]. The real mass flow of each nozzle was calculated using critical flow Venturi meters conforming to ISO9300 [37] within the high-pressure air systems. The "ideal" mass flows were calculated based on the P_0 and T_0 rake measurements upstream of the nozzles within fan and core streams (Fig. 3). Four (4) azimuthally equispaced rakes with twelve (12) probes each were used to measure the P_0 distribution at

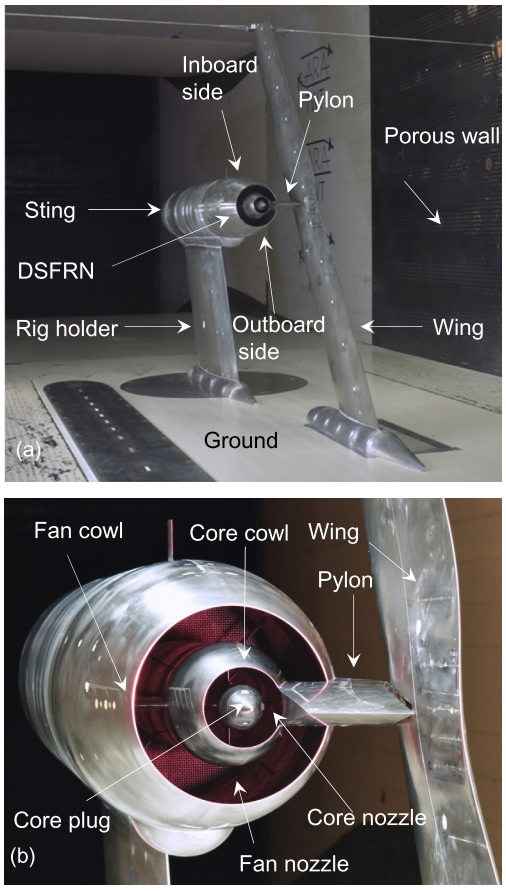


Fig. 1. ARA Dual Stream Jet Propulsion (DSJP) rig: (a) General view of installed configuration in the wind tunnel and (b) Close-up of Dual Separate Flow Reference Nozzle (DSFRN).

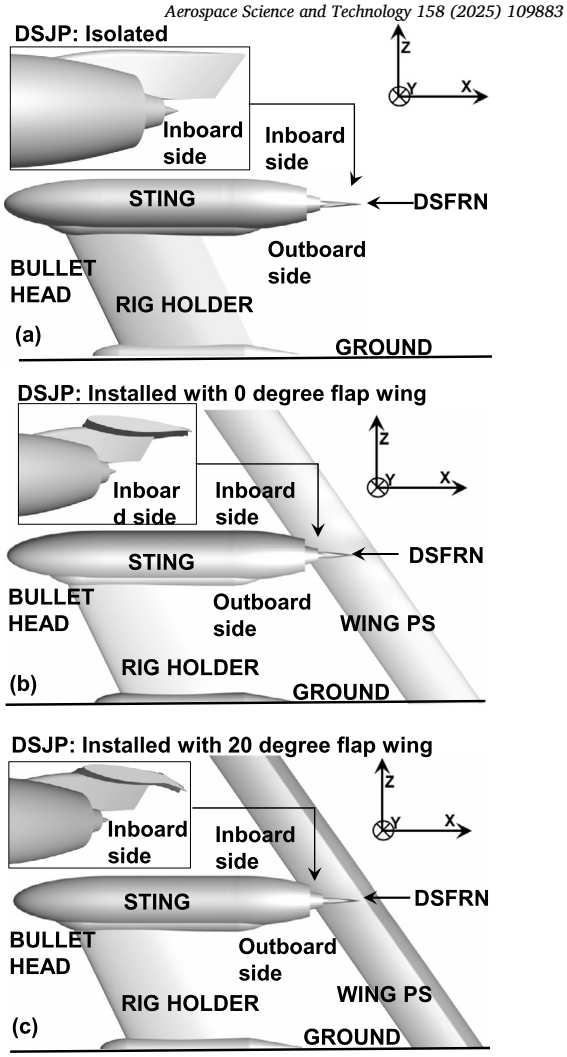


Fig. 2. ARA Dual Stream Jet Propulsion (DSJP) rig geometry [28]: (a) isolated configuration (wing-off), (b) installed configuration with 0 degree flap wing (clean wing-on) and (c) installed configuration with 20 degree flap wing (20 degree flap wing-on).

entry to the fan nozzle (Fig. 3). Four (4) azimuthally equispaced rakes with five (5) probes each were used for the core inlet P_0 measurement. The P_0 probe measurement errors were $\approx 0.15\%$ and $\approx 0.03\%$ for the fan and core rakes, respectively, within a 95% confidence interval. The fan and core rake P_0 values were acquired using a Digital Thermal Compensation (DTC) pressure scanner. The data was acquired at 10 Hz for 4.8 seconds which were subsequently averaged to produce a single value for each condition.

A statistical analysis was carried out to quantify the experimental measurement uncertainty for C_d^{Fan} and C_d^{Core} based on Monte-Carlo simulation [38]. The measurement uncertainty of the pressure and temperature sensors within the airlines and the rig were assumed independent and normally distributed. The analysis included 2×10^4 samples to ensure that the mean (μ) and standard deviation (σ) values of the measurement error distribution converged deterministically. With these provisions, the measurement errors for C_d^{Fan} and C_d^{Core} were estimated to be approximately $\pm 0.15\%$ within a 95% confidence interval.

2.3. Engine performance simulation methodology

A Zero-Dimensional (0D) engine performance simulation model was implemented to estimate the impact of installed exhaust suppression on the engine airflow and MFCR. The engine model had a BPR of 10 at mid-cruise, which is similar to that of the DSFRN [26,19]. The platform for this model was the NASA Numerical Propulsion System Simulation (NPSS) [35] which analyses the aero-thermal behaviour of the powerplant. NPSS is based on 0D analysis of gas turbine engines using discrete component maps. NPSS solves for the mass and energy balance between the various engine components. A non-linear "matrix-iteration" method based on the Newton-Raphson scheme [39] is used for OD analyses [35].

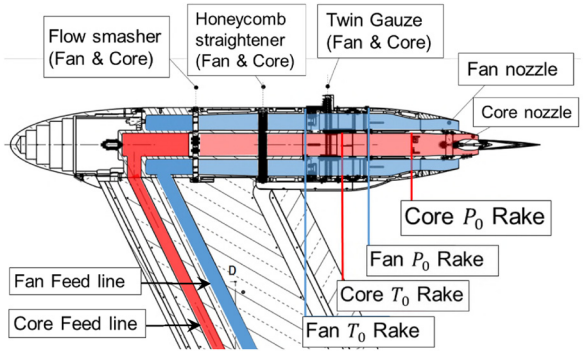


Fig. 3. Internal flow structure of ARA Dual Stream Jet Propulsion (DSJP) rig: Core flow (red) and bypass flow (blue). (For interpretation of the colours in the figure(s), the reader is referred to the web version of this article.)

This scheme is used to solve the non-liner equations that satisfy the matching constraints in terms of turbine and nozzle non-dimensional flow capacities. This process establishes the total pressure (P_0) and temperature (T_0) at the entry of the fan and core nozzles, as well as the engine mass flow.

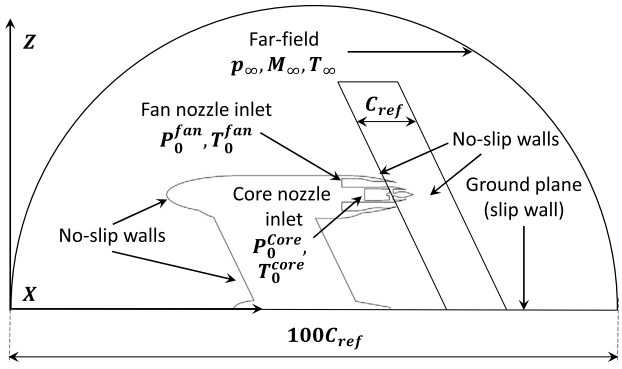


Fig. 4. Schematic of computational domain and boundary conditions (not to scale) [28].

A novel aspect of this NPSS model is that it uses fan and core compressor maps that were derived specifically for sub-idle engine modelling. These component maps were defined based on the consolidation between experimental measurements and simulations [31–33]. The map derivation method was based on the method of "locked-rotor" map interpolation which defines the fan and core compressor performance characteristics down to sub-idle operating regimes. Therefore, the fan and compressor component maps used in the NPSS model were appropriate for wind-milling analysis.

The measured and predicted fan and core nozzle performance maps were implemented in NPSS. The maps expressed C_d^{Fan} and C_d^{Core} as functions of M_∞, FNPR, and CNPR for the DSJP configurations (Fig. 2): (a) "Isolated", (b) "clean wing", and (c) "20-degree flap wing". The NPSS model was subsequently used to estimate the impact of installed suppression on wind-milling engine air mass-flow and MFCR for EOR, diversion, and mid-cruise conditions.

2.4. Computational fluid dynamics approach

The RANS CFD methodology was described in detail by Goulos et al. [28]. A far-field type Boundary Condition (BC) was used to avoid the complexity of modelling the TWT wall porosity [27]. A hemispherical domain was used with a diameter of $100 \times C_{ref}$, where C_{ref} is the reference DSJP wing chord length (Fig. 4). The free-stream flow conditions were modelled with prescribed p_∞, M_∞, and T_∞ at the hemispherical far-field boundary (Fig. 4). The fan and core nozzle inlet boundaries were modelled as pressure inlet BCs with defined P_0 and T_0 (Fig. 4). All surfaces were modelled as adiabatic and viscous no-slip walls, with the exception of the tunnel floor which was modelled as a slip wall.

A hybrid meshing methodology was used [40] with structured prism layers near the viscous walls with $y^+ < 1$ for all wall-adjacent nodes. Unstructured tetrahedral elements were used for the remainder of the computational domain. Near-wall unstructured mesh refinement was performed based on local wall-curvature and surface-proximity features [40]. Unstructured mesh refinement zones were defined in the vicinity of the exhaust, pylon, and wing to resolve localised flow features. The spatial discretisation was based on the grid verification activities. These showed that the hybrid meshes required approximately 50 million and 100 million elements for the isolated and installed cases, respectively. Specifically, for the installed configuration (Fig. 2(b)), the differences in C_d^{Fan} and C_d^{Core} were 0.03% and 0.08% at DP ($M_\infty = 0.85$, $FNPR = 2.4$, and $CNPR = 2.0$), respectively, between meshes with 100 and 200 million elements.

The analyses used an implicit, density-based, and compressible Favre averaged CFD approach [41] coupled with the $k-\omega$ Shear-Stress Transport (SST) turbulence model [42]. The flow-field gradients were calculated based on the Green-Gauss node-based method. A second-order accurate upwind scheme was used for the spatial discretisation of primitive variables, turbulent kinetic energy k, and specific dissipation rate ω. Kinetic theory was used to calculate thermal conductivity κ [41]. Variable gas properties were used based an 8^{th} order piecewise polynomial expression for the calculation of specific heat capacity [11]. Dynamic viscosity was calculated using Sutherland's law [43].

The computational approach was previously validated [12] based on the experimental data of Mikkelsen et al. [26] for the DSFRN. Analyses were carried out for an FNPR range ($FNPR = \frac{P_0^{Fan}}{p_\infty}$) between 1.4 and 2.8 and for ground-level static conditions ($M_\infty \approx 0$). A fixed Extraction Ratio was used with ($ER = \frac{FNPR}{CNPR} = 1.2$), where $CNPR = \frac{P_0^{Core}}{p_\infty}$. The Root Mean Square (RMS) difference between CFD predictions and measurements, was almost 0.04%, 0.30%, and 0.42% for C_v, C_d^{Fan}, and C_d^{Core}, respectively.

2.5. Definition of exhaust system performance metrics

The definitions of C_d^{Fan} and C_d^{Core} for the DSFRN wind-tunnel tests were provided by Mikkelsen et al. [26] and used by Gomariz-Sancha et al. [25] for the DSJP rig (Fig. 1). These definitions are also used in this work to ensure consistency with the standard accounting of Mikkelsen et al. [26].

The nozzle discharge coefficients are defined as the ratio of the actual nozzle mass flow over the ideal mass flow ($\dot{m}_{Ideal}$) resulting from isentropic expansion to ambient static pressure [26]. The ideal nozzle mass flow (Eq. (1)) for specified values of P_0 and T_0 at the nozzle inlet boundary (Fig. 4) is given by:

$$\dot{m}_{Ideal} = A_{throat} P_0 \left(\frac{1}{\lambda}\right)^{\frac{1}{\gamma}} \sqrt{\frac{2\gamma}{(\gamma-1)RT_0}\left(1-\left(\frac{1}{\lambda}\right)^{\frac{\gamma-1}{\gamma}}\right)} \tag{1}$$

where $\lambda = \frac{P_0}{P_{amb}}$ is the nozzle inlet total to ambient static pressure ratio, A_{throat} is the nozzle throat area, p_∞ is the ambient static pressure, R is the gas constant for air, and γ is the ratio of specific heats. It is noted that for $\lambda \geq \lambda_{crit} = \left(\frac{\gamma+1}{2}\right)^{\frac{\gamma}{\gamma-1}}$, the value of λ_{crit} is used in Eq. (1) instead of λ. The fan and core nozzle discharge coefficients can be written as follows:

$$C_d^{Fan} = \frac{\dot{m}_{CFD}^{Fan}}{\dot{m}_{Ideal}^{Fan}} \qquad C_d^{Core} = \frac{\dot{m}_{CFD}^{Core}}{\dot{m}_{Ideal}^{Core}} \tag{2}$$

where the values of $\dot{m}_{CFD}^{Fan}$ and $\dot{m}_{CFD}^{Core}$ in Eq. (2) are obtained by integrating the mass fluxes across the fan and core nozzle entry planes (Fig. 4).

3. Results and discussion

3.1. Installed suppression test configurations and operating conditions overview

Table 1 summarises the configurations (Fig. 2) and range of operating conditions for the experimental and computational activities. The test program cases generally lie within the low FNPR and CNPR regimes. This is because the main aim of the installed suppression test was to cover the wind-milling regime. This was defined based on a combination of NPSS simulations [35], computational analyses [28], and low-order modelling based on Low-Pressure (LP) system loss coefficients found in the literature [9,44]. For the experimental and computational studies a total of 458 cases were investigated encompassing isolated and installed configurations.

Table 1
Summary of computational and experimental operating conditions and configurations.

Designation	M_∞	Configuration	$FNPR$ CFD	$CNPR$ CFD	$FNPR$ Exp.	$CNPR$ Exp.
Wind-milling EOR (1)	0.20	Isolated Inst. clean wing Inst. 20-deg flap	[1.02-1.20]	[1.02-1.09]	[1.02-1.20]	[1.02-1.09]
Wind-milling EOR (2)	0.35	Isolated Inst. clean wing Inst. 20-deg flap	[1.03-1.20]	[1.03-1.09]	[1.03-1.20]	[1.03-1.09]
Wind-milling Diversion	0.65	Isolated Inst. clean wing	[1.10-1.40]	[1.08-1.30]	[1.15-1.33]	[1.08-1.27]
Wind-milling Cruise	0.85	Isolated Inst. clean wing	[1.40-2.80]	[1.17-2.33]	[1.4-2.60]	[1.17-2.16]

3.2. Installed fan and core nozzle suppression validation

Fig. 5 presents the measured and predicted suppression effect of the fan nozzle. Results are presented in terms of $(C_{d,installed}^{Fan} - C_{d,isolated}^{Fan})(\%)$ as a function of FNPR and M_∞. The circular and triangular markers correspond to the 0-degree flap wing (clean wing), and 20-degree flap wing, respectively. The full and empty markers correspond to predictions and experimental data, respectively. All markers are coloured by M_∞ to distinguish the EOR ($M_\infty = 0.20$ and $M_\infty = 0.35$), diversion ($M_\infty = 0.65$), and cruise cases ($M_\infty = 0.85$). Results are presented for the entire set of investigated conditions (Table 1) in Fig. 5(a), whilst a close-up at the EOR cases is shown in Fig. 5(b).

The effect of installed suppression increases markedly with reducing FNPR. The installed fan nozzle suppression effect is maximum for the EOR case with $M_\infty = 0.35$ and the 20-degree flap wing for which the effect can reach up to -26% for FNPR = 1.03, according to the experimental data. This reduces to approximately -13% for a slight increase in the FNPR to 1.05. This highlights the strong dependency of the installed suppression on FNPR for wind-milling conditions. Furthermore, the suppression increases considerably for the 20-degree flap wing relative to the 0-degree flap arrangement. For example, switching from the 0-degree flap wing to the 20-degree flap wing at $M_\infty =$ 0.35 the measured suppression increases from -9% to approximately -26%. This highlights the strong impact of the 20-degree flap on C_d^{Fan} (Fig. 5(b)).

Figs. 5(a) and (b) also show that M_∞ has a significant impact on the installed C_d^{Fan} suppression. For the 20-degree flap wing and at a fixed FNPR = 1.03, the measured ΔC_d^{Fan} increases from -7% to -26% for increasing M_∞ from 0.20 to 0.35. This is due to the increased wing lift at higher M_∞ which leads to an increase the local wing static pressure which suppresses the fan nozzle mass flow. Furthermore, the potency of the effect of M_∞ on the installed fan nozzle suppression is dependent on the wing configuration. Finally, it is noted that the suppression of the fan nozzle is not influenced by CNPR changes.

Overall, there is very good agreement between predictions and measurements across the range of operating conditions. The Root Mean Square Deviation (RMSD) across the range of conditions varies between 0.1% and 1.2% depending on wing configuration and M_∞ (Table 2). In general the CFD slightly under-predicts the installed suppression effect in the low FNPR range ($FNPR \leq 1.05$) when the 20-degree flap wing is deployed. The maximum difference of the installed C_d^{Fan} suppression between the computations and measurements is of the order -2.2% for $M_\infty = 0.35$ with the 20-degree flap. This is an order of magnitude smaller than the suppression effect which is approximately -26%.

Fig. 6 presents the installed core nozzle suppression in terms of $(C_{d,installed}^{Core} - C_{d,isolated}^{Core})(\%)$ as a function of CNPR and M_∞. The circular and triangular markers correspond to the 0-degree flap wing (clean wing), and 20-degree flap wing, respectively. The full and empty markers correspond to numerical predictions and experimental data, respectively. All markers are coloured by M_∞. Overall, there is very good agreement between predictions and experimental data. The RMSD across the range of conditions varies between 0.41% and 1.7% depending on wing configuration and M_∞ (Table 2). The aerodynamic mechanisms that govern the behaviour of the installed C_d^{Core} suppression effects are similar to those described for C_d^{Fan}, therefore further elaboration is omitted.

3.3. Installed fan and core nozzle suppression maps

Fig. 7, Fig. 8, and Fig. 9 present comparisons between numerical predictions and experimental data for installed C_d^{Fan} and C_d^{Core} suppression corresponding to EOR (1), EOR (2), and diversion wind-milling conditions (Table 1), respectively. Results are shown for the 20-degree flap wing in Fig. 7 and Fig. 8, whilst the 0-degree flap wing (clean wing) is used for the diversion case in Fig. 9.

The numerical predictions capture the character of installed fan and core nozzle suppression well across all investigated wind-milling conditions (Figs. 7-9). The impact of both FNPR and CNPR is well predicted across the evaluated envelopes (Table 1) for both C_d^{Fan} and C_d^{Core}. However, CFD generally under-predicts the magnitude of installed suppression for both nozzles. For the fan nozzle, the RMSD of this under-prediction across the ranges of FNPR and CNPR, is about 0.8%, 1.2%, and 0.2% for $M_\infty = 0.20$, $M_\infty = 0.35$, and $M_\infty = 0.65$, respectively, with similar numbers observed for the core nozzle (Table 2).

Figs. 7 and 8 show that M_∞ has a notable effect on the installed C_d^{Fan} and C_d^{Core} suppression. For the 20-degree flap wing, the maximum fan nozzle suppression increases from -11% to -26% for increasing M_∞ from 0.20 to 0.35, according to the experimental data (Fig. 7(b) and Fig. 8(b)). This is due to the increasing static pressure disturbance from the wing Pressure Side (PS) with increasing M_∞ which propagates to pressurise the fan nozzle and after-body surfaces, and suppresses the fan nozzle mass flow. A similar behaviour is noted for C_d^{Core} due to the increased pressurisation of the core nozzle and cowl surfaces stemming from the amplified impact of the wing and flap at $M_\infty = 0.35$

The impact of FNPR on the installed core nozzle suppression is also evident for the EOR wind-milling cases in Figs. 7(c), (d) and Figs. 8(c), (d). Specifically, at fixed CNPR and M_∞, an increase in FNPR results in an increase of core flow suppression. This is due to the higher fan suppression effect on the core with increasing FNPR which reduces the core nozzle jet mass and momentum efflux at fixed CNPR and M_∞. This amplifies the core nozzle's sensitivity to the installed pressure field. The core nozzle suppression because of the fan stream is negligible for the diversion case (Figs. 9(c) and (d)) due to the higher CNPR.

3.4. Installed exhaust suppression aerodynamic mechanisms

Goulos et al. [28] demonstrated that the installed C_d^{Fan} suppression mechanisms for the 0-degree and 20-degree flap wings are notably different. For the 0-degree flap wing (Fig. 9) the installed suppression effect

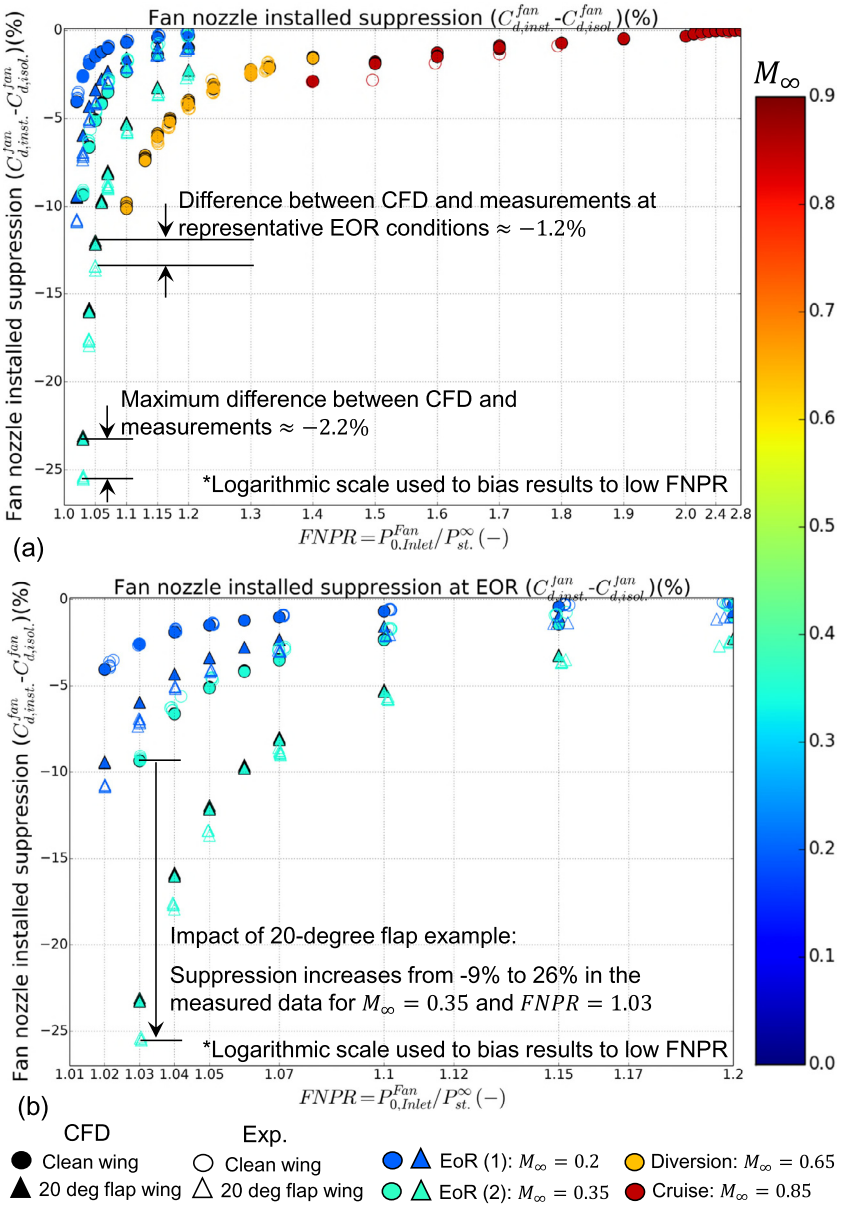


Fig. 5. Impact of FNPR and M_∞ on installed fan nozzle suppression effect ($C^{Fan}_{d,installed} - C^{Fan}_{d,isolated}$)(%): (a) Entire set of investigated operational envelope and (b) Close-up of EOR conditions and impact of 20-degree flap example (multiple CNPR points included).

Table 2
Summary of installed fan and core nozzle suppression CFD validation results.

Designation	M_∞	Configuration	RMSD (Exp.-CFD) ($C^{Fan}_{d,installed} - C^{Fan}_{d,isolated}$)(%)	RMSD (Exp.-CFD) ($C^{Core}_{d,installed} - C^{Core}_{d,isolated}$)(%)
WM EOR (1)	0.20	Inst. clean wing	0.10%	0.41%
	0.20	Inst. 20-deg flap	0.83%	0.67%
WM EOR (2)	0.35	Inst. clean wing	0.54%	0.79%
	0.35	Inst. 20-deg flap	1.20%	1.70%
WM Diversion	0.65	Inst. clean wing	0.17%	1.12%
WM Cruise	0.85	Inst. clean wing	0.37%	0.85%

manifests through a mass flux reduction near the fan nozzle exit outboard side [28]. This is due to the closer proximity of the wing leading edge stagnation point to the fan nozzle outboard side because of the wing sweep angle (Fig. 2). The high-static pressure due the wing LE stagnation point propagates to pressurize the fan nozzle base on the outboard side top-line which suppresses the local mass flux.

For the 20-degree flap wing (Figs. 7 and 8), the installed C^{Fan}_{d} suppression effect stems due to a mass-flux reduction near the fan nozzle

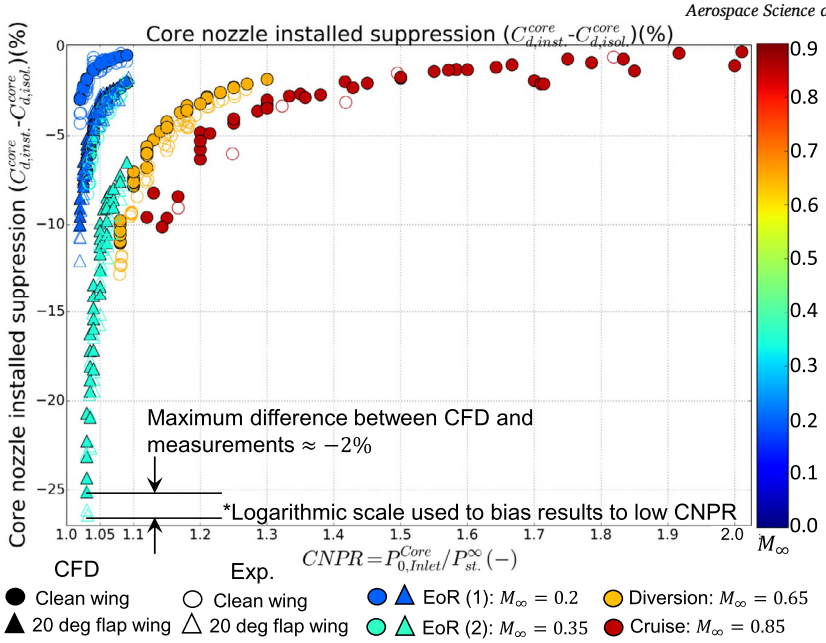


Fig. 6. Impact of CNPR and M_∞ on installed core nozzle suppression effect $(C^{Core}_{d,installed} - C^{Core}_{d,isolated})(\%)$ including comparisons between CFD and experimental data (multiple FNPR points included).

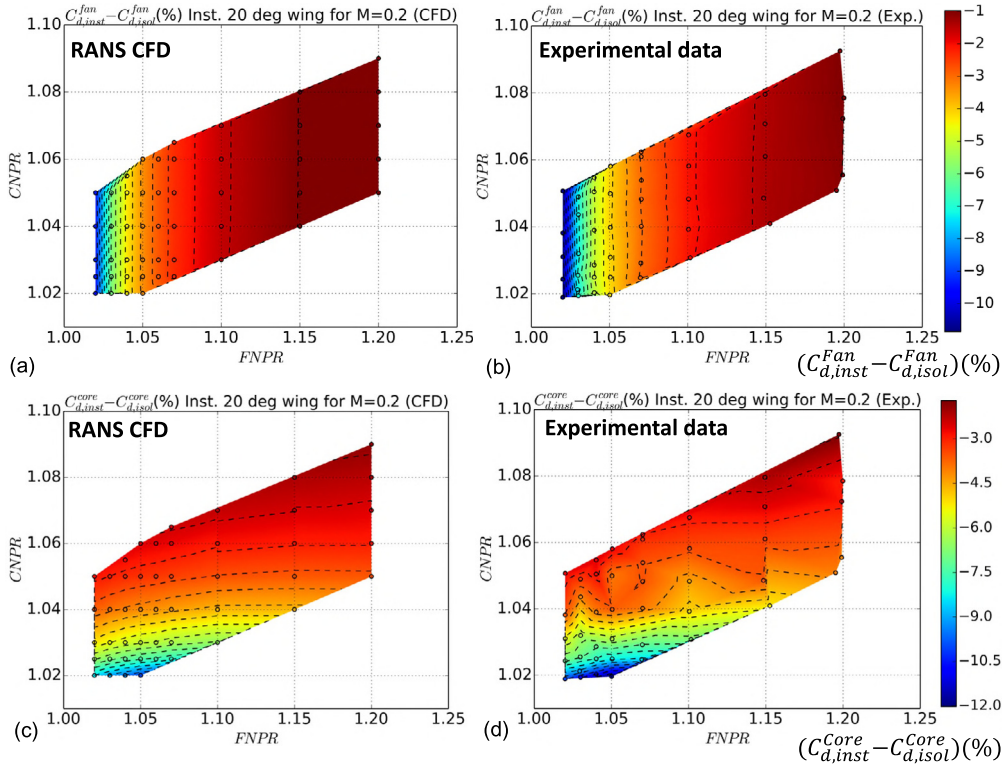


Fig. 7. Installed exhaust suppression $(C^{Fan/Core}_{d,installed} - C^{Fan/Core}_{d,isolated})(\%)$ at wind-milling EOR (1) for 20-degree flap wing and $M_\infty = 0.20$: (a) Fan nozzle CFD, (b) Fan nozzle Exp., (c) Core nozzle CFD, (d) Core Nozzle Exp.

exit inboard side. This is due to the static pressure rise on the wing PS due to the presence of the flap which propagates upstream to pressurise the fan nozzle base. The wing trailing edge flap is closer to the fan nozzle exit on the inboard side, relative to the outboard side due to the swept wing arrangement (Fig. 2). Therefore, the fan nozzle base pressurization is more potent for the inboard side compared to the outboard side, leading to a higher local mass flux suppression [28]. The fundamental aerodynamic mechanisms that govern the installed suppression effect for the fan and core streams were exposed in detail by Goulos et al. [28].

3.5. CFD validation of exhaust nozzle discharge coefficients

The numerical approach used in this work was also validated in terms of its ability to predict absolute values of C^{Fan}_d and C^{Core}_d across the investigated range of operating conditions (Table 1). The RMSD be-

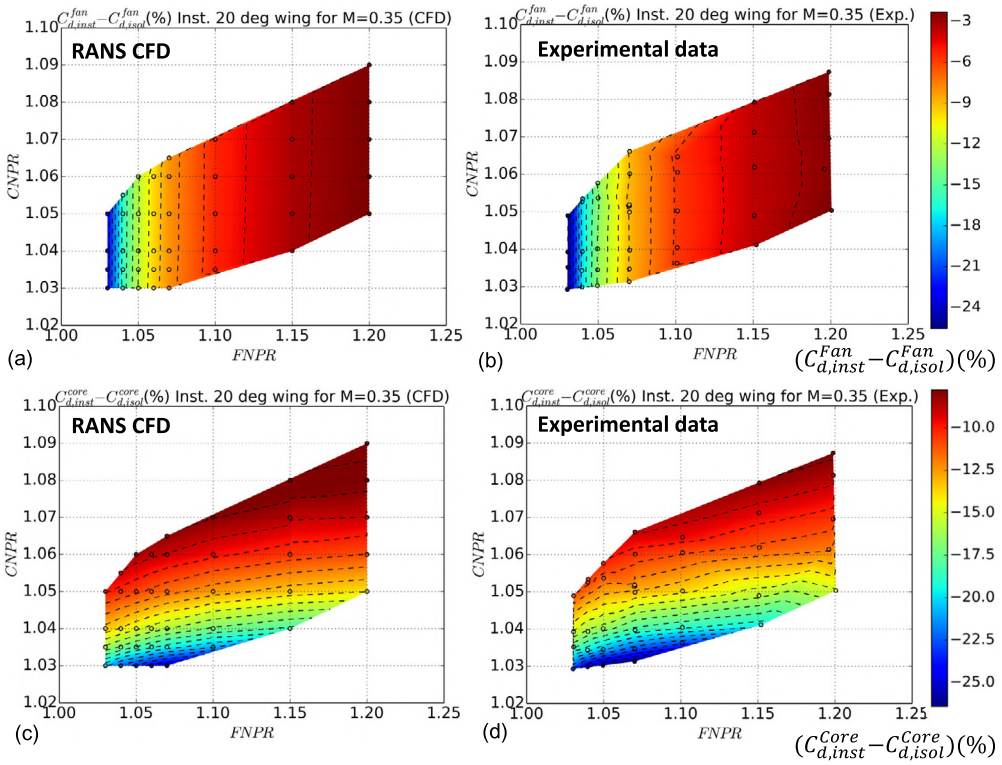


Fig. 8. Installed exhaust suppression $(C^{Fan/Core}_{d,installed} - C^{Fan/Core}_{d,isolated})(\%)$ at wind-milling EOR (2) for 20-degree flap wing and $M_\infty = 0.35$: (a) Fan nozzle CFD, (b) Fan nozzle Exp., (c) Core nozzle CFD, (d) Core Nozzle Exp.

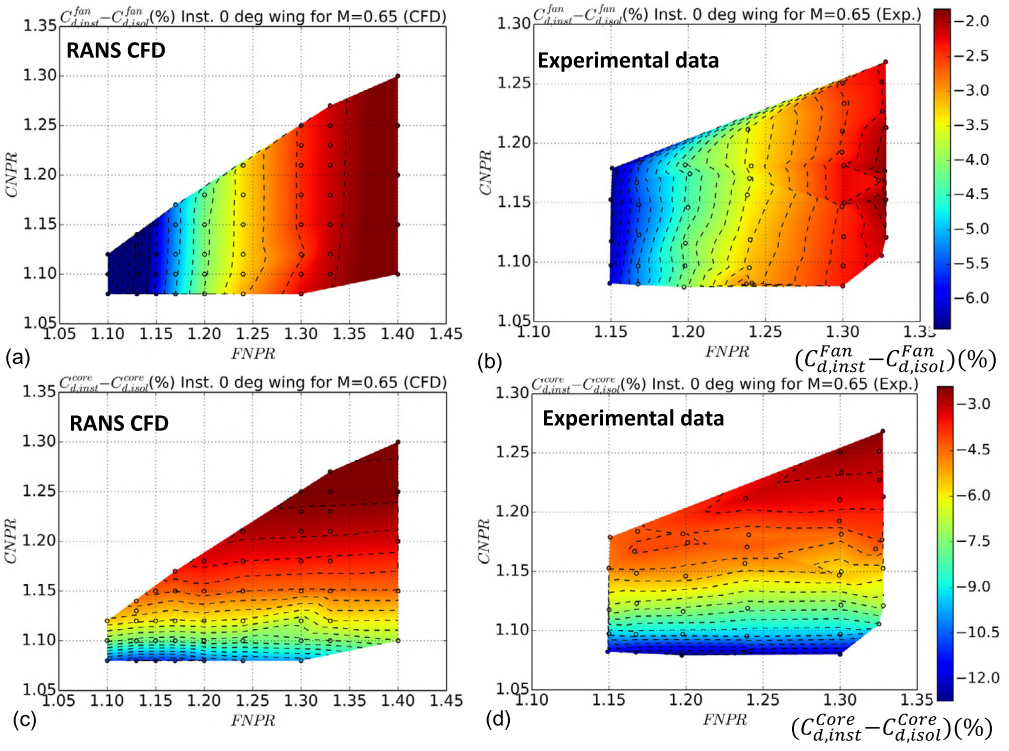


Fig. 9. Installed exhaust suppression $(C^{Fan/Core}_{d,installed} - C^{Fan/Core}_{d,isolated})(\%)$ at wind-milling diversion for 0-degree flap wing and $M_\infty = 0.65$: (a) Fan nozzle CFD, (b) Fan nozzle Exp., (c) Core nozzle CFD, (d) Core Nozzle Exp. (larger FNPR and CNPR ranges used for CFD).

tween CFD predictions and experimental data for each configuration and condition are summarised in Table 3. A graphical comparison between predictions and experimental measurements is presented in Figs. 10 and 11.

CFD simulations generally under-predict both C_d^{Fan} and C_d^{Core} relative to the experimental data across the range of conditions. The RMSD between CFD predictions and experimental data is of the order of 0.96% and 0.91% for C_d^{Fan} and C_d^{Core}, respectively, for the installed clean wing

Table 3
Summary of CFD validation for installed and isolated C_d^{Fan} and C_d^{Core}.

Designation	M_∞	Configuration	FNPR Range (Exp.)	RMSD RMSD ($C_{d,Exp.}^{Fan} - C_{d,CFD}^{Fan}$)(%)	CNPR Range (Exp.)	RMSD RMSD ($C_{d,Exp.}^{Core} - C_{d,CFD}^{Core}$)(%)
WM EOR (1)	0.20	Inst. clean wing Inst. 20-deg flap Isolated	[1.02-1.20]	5.58% 4.79% 5.56%	[1.02-1.09]	0.97% 0.86% 1.16%
WM EOR (2)	0.35	Inst. clean wing Inst. 20-deg flap Isolated	[1.03-1.20]	4.93% 3.36% 4.51%	[1.03-1.09]	1.02% 0.51% 1.69%
WM Diversion	0.65	Inst. clean wing Isolated	[1.15-1.33]	2.82% 2.91%	[1.08-1.27]	1.03% 1.87%
WM Cruise	0.85	Inst. clean wing Isolated	[1.40-2.60]	0.96% 1.38%	[1.17-2.16]	0.91% 1.28%

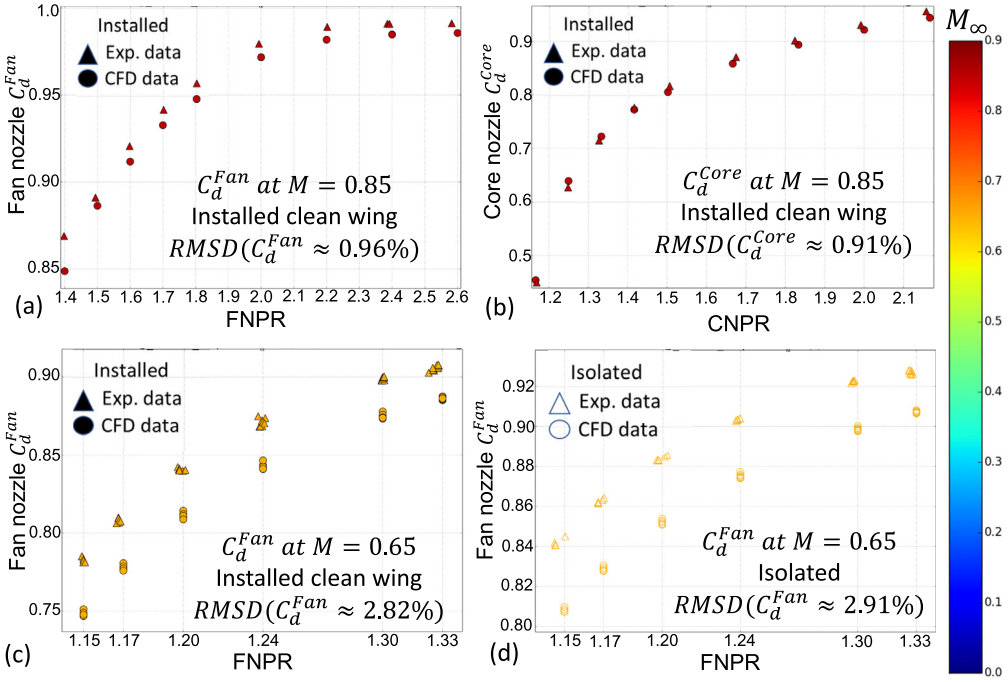


Fig. 10. CFD validation for exhaust performance at mid-cruise and diversion conditions: (a) Installed clean wing C_d^{Fan} at $M_\infty = 0.85$, (b) Installed clean wing C_d^{Core} at $M_\infty = 0.85$, (c) Installed clean wing C_d^{Fan} at $M_\infty = 0.65$, (d) Isolated C_d^{Fan} at $M_\infty = 0.65$ (markers coloured as per M_∞, multiple CNPR points included).

configuration at $M_\infty = 0.85$ and $FNPR \in [1.4 - 2.8]$ (Figs. 10(a) and (b)). Similar RMSDs of the order of 1.28% and 1.38% can be noted for C_d^{Fan} and C_d^{Core}, respectively, for the isolated exhaust at $M_\infty = 0.85$ and same FNPR range (Table 3). These differences between CFD simulations and experimental measurements are approximately 0.6% higher compared to those noted during "wind-off" testing for the DSFRN [26] and published in the existing literature [19,12]. However, previous validation efforts have not accounted for the "installation" and "wind-on" effects that are analysed in this work and affect the aerodynamic behaviour of the exhaust.

Figs. 10, 11 and Table 3 show that the RMSD between numerical predictions and experimental measurements increase with reducing M_∞ and FNPR. The RMSD for C_d^{Fan} increases from 0.96% to 4.79% for reducing M_∞ from 0.85 to 0.2, and for reducing the FNPR range from [1.4-2.6] to [1.02-1.20], which corresponds to the EOR wind-milling range with the 20-degree flap wing installed. Figs. 10 and 11 show that the CFD under-predicts C_d^{Fan} and that this increases with reducing FNPR and M_∞. A similar behaviour is observed for the isolated exhaust configuration. This demonstrates the deteriorated performance of CFD in obtaining accurate absolute values of C_d^{Fan} for the EOR wind-milling range of exhaust inlet conditions (Figs. 11(a)-(d)).

The effect of fan nozzle inlet turbulence intensity (Tu_{in}) was investigated to assess whether it was the cause of the deviation between CFD and measurements of C_d^{Fan} at lower values of FNPR (Table 3). A value of $Tu_{in} = 1\%$ was used for all CFD analyses reported in this work. The Tu_{in} at the fan nozzle inlet was not measured. In the absence of these measurements, CFD analyses were carried out to understand the impact of inlet Tu_{in} on C_d^{Fan} for representative EOR wind-milling conditions ($M_\infty = 0.35$, FNPR = 1.05, CNPR = 1.03). It was found that a change of fan nozzle inlet Tu_{in} from 0.1% to 10% results in a reduction of C_d^{Fan} of the order of 0.1%. Therefore, any variations in Tu_{in} were not responsible for the deviations in C_d^{Fan} between CFD and measurements.

With regards to the C_d^{Core} RMSD, Table 3 shows that this is relatively unaffected with reducing M_∞ and CNPR, relative to the cruise conditions at $M_\infty = 0.85$. Specifically, the C_d^{Core} RMSD reduces slightly from 0.91% to 0.86% for reducing M_∞ from 0.85 to 0.2, and for reducing the CNPR range from [1.17-2.16] to [1.02-1.09], which is the EOR wind-milling range (20-degree flap wing installed). A similar observation applies with regards to isolated exhaust predictions where the C_d^{Core}

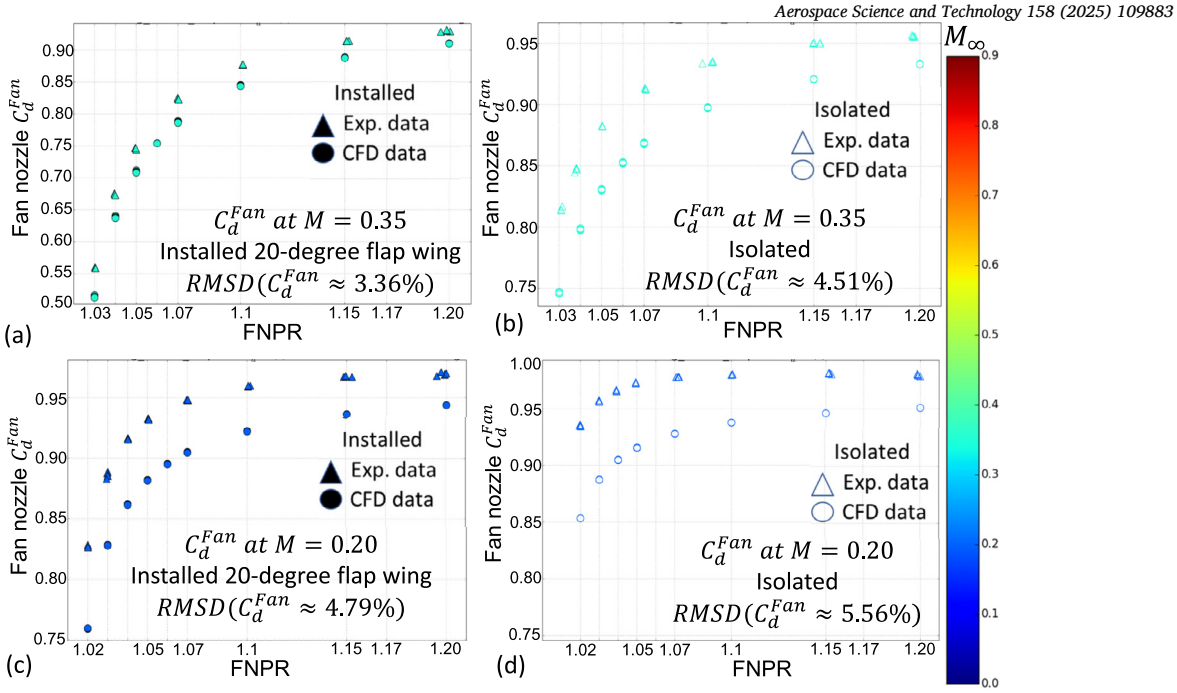


Fig. 11. CFD validation for exhaust performance at EOR conditions: (a) Installed 20-degree flap wing C_d^{Fan} at $M_\infty = 0.35$, (b) Isolated C_d^{Fan} at $M_\infty = 0.35$, (c) Installed 20-degree flap wing C_d^{Fan} at $M_\infty = 0.20$, (d) Isolated C_d^{Fan} at $M_\infty = 0.20$ (markers coloured as per M_∞, multiple CNPR points included).

RMSD between simulations and experimental measurements appears to be unaffected by the CNPR range and M_∞.

3.6. Exhaust and wing static pressure distributions

The computational approach was further validated in terms of its ability to predict the static pressure distribution on the exhaust, wing, and pylon surfaces. Figs. 12 and 13 compare the computations and measurement of the local static pressure coefficient $C_p^{mod} = \frac{p - p_\infty}{p_\infty}$ at EOR wind-milling conditions with $M_\infty = 0.35$, FNPR = 1.05, and CNPR = 1.03. Results are presented for the fan and core cowl C_p^{mod} distributions in Figs. 12 and 13, respectively. The C_p^{mod} surface distributions predicted by CFD are illustrated in Fig. 14 along with the sampling regions for which comparisons with experimental data are presented in Figs. 12 and 13. Results are shown for the isolated and 20-degree flap wing installed configurations in Figs. 12, 13(a) and Figs. 12, 13(b), respectively.

CFD predictions agree well with experimental measurements of fan cowl static pressure distributions (Fig. 12) for both isolated and installed arrangements. The maximum difference (Δ) for C_p^{mod} is of the order 0.15% and 0.2% for the isolated (Fig. 12(a)) and 20-degree flap wing installed configurations (Fig. 12(b)), respectively. For the isolated exhaust (Fig. 12(a)), the CFD captures well the rise in static pressure along the fan cowl axial coordinate as the flow approaches the fan cowl trailing edge. Furthermore, a small rise on the outboard side static pressure can be observed due to the presence of the rig support sting. Generally, the circumferential variations in fan cowl static pressure due to the rig mount effects are predicted well by the CFD.

For the 20-degree flap configuration, Fig. 12(b) shows that there is notable inboard-outboard asymmetry of static pressure near the fan cowl top line. This is due to the closer proximity of the flap to the fan cowl trailing edge on the inboard side, relative to the outboard side due to the sweep angle of the wing which is around 34 degrees. This inboard-outboard asymmetry in static pressure due to the impact of installation (Fig. 14) is well captured by the CFD and the maximum delta between predictions and measurements is approximately 0.2%.

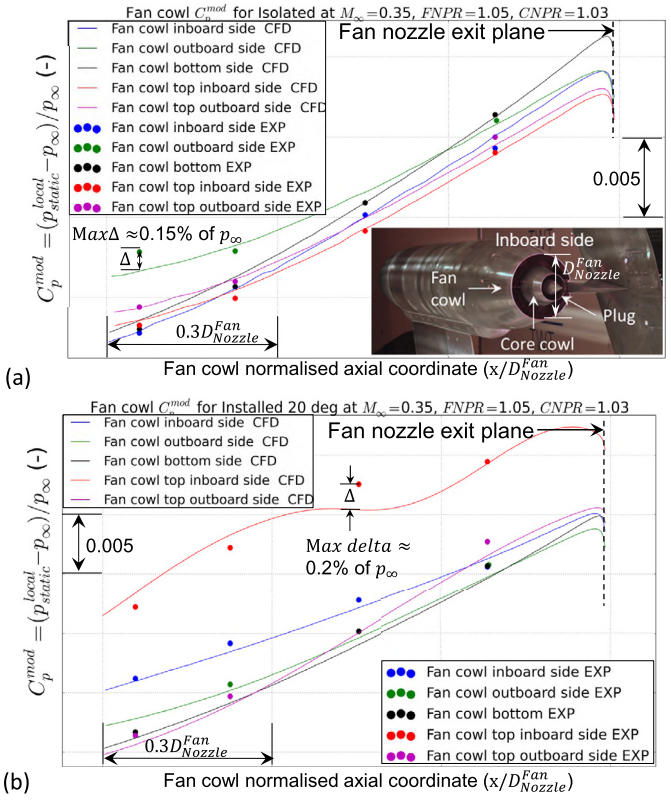


Fig. 12. Normalised fan cowl static pressure distribution $C_p^{mod} = \frac{p - p_\infty}{p_\infty}$ at EOR wind-milling conditions with $M_\infty = 0.35$, FNPR = 1.05, and CNPR = 1.03: (a) Isolated configuration and (b) Installed with 20-degree flap wing.

Fig. 13 compares predictions and measurements of C_p^{mod} on the core cowl for the same EOR wind-milling condition as in Fig. 12. Results are presented for the isolated and 20-degree flap wing installed configurations in Fig. 13(a) and (b), respectively. Predictions and measurements

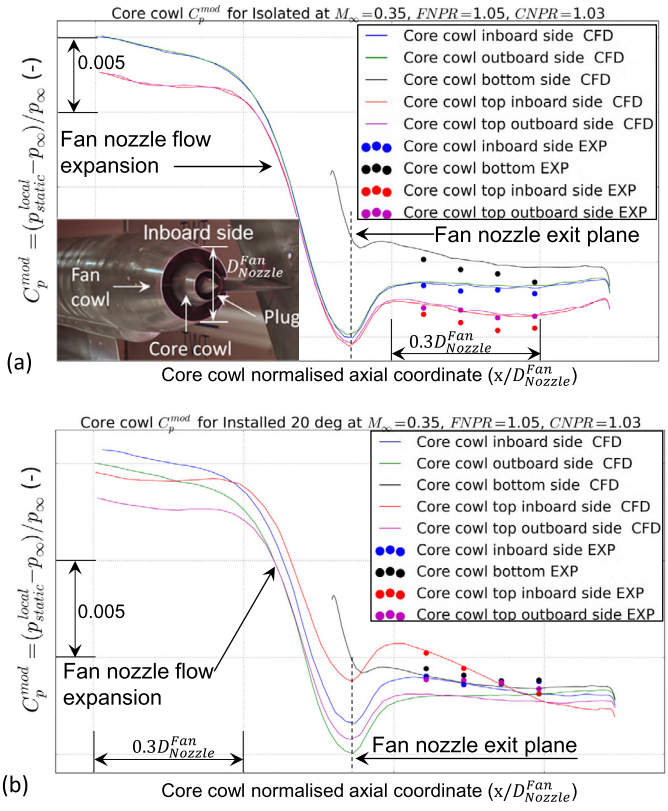


Fig. 13. Normalised core cowl static pressure distribution $C_p^{mod} = \frac{p - p_\infty}{p_\infty}$ at EOR wind-milling conditions with $M_\infty = 0.35$, FNPR = 1.05, and CNPR = 1.03: (a) Isolated configuration and (b) Installed with 20-degree flap wing.

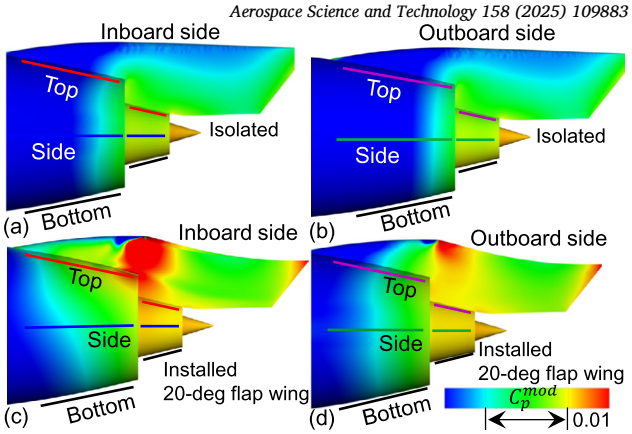


Fig. 14. Normalised fan and core cowl static pressure distribution $C_p^{mod} = \frac{p - p_\infty}{p_\infty}$ at EOR wind-milling conditions with $M_\infty = 0.35$, FNPR = 1.05, and CNPR = 1.03: (a) Isolated inboard side, (b) Isolated outboard side, (c) Installed with 20-degree flap wing inboard side, (d) Installed with 20-degree flap wing outboard side.

of core cowl C_p^{mod} agree within almost 0.1% and 0.07% on average for the isolated (Fig. 13(a)) and 20-degree flap wing installed configuration (Fig. 13(b)), respectively. A small asymmetry in C_p^{mod} between the top inboard and top-outboard side is present for the installed configuration ($\Delta C_p^{mod} \leq 0.15\%$) (Fig. 13(b)) due to the effect of the swept wing and flap. This lateral asymmetry in C_p^{mod} is captured by the CFD within 0.05% of the measured data.

A notable increase in the CFD predicted C_p^{mod} can be observed upstream of the fan nozzle exit plane (Figs. 13(a) and (b)) which is due to the increase in static pressure in the bypass duct. The C_p^{mod} variation in this region depends on the fan nozzle mass flow and concurrently on C_d^{Fan}. Unfortunately, there were no static pressure tappings within the bypass duct and fan nozzle to establish a direct comparison between experimental data and CFD. The agreement between the measurements and the CFD in this region is reflected in the absolute values of C_d^{Fan}, which are driven by the fan nozzle mass flow. This is shown in Figs. 11(a) and (b) where the CFD under-predicts C_d^{Fan} by between 3.36% to 4.51%, installed and isolated, respectively. CFD generally over-predicts the core after-body C_p^{mod} variation by almost 0.1% of p_∞ for the isolated nozzle (Fig. 13(a)). This C_p^{mod} over-prediction of 0.1% is very small and not sufficient to cause these differences between measured and predicted C_d^{Fan}.

Fig. 15 presents the CFD validation for the wing flow topology in terms of isentropic Mach number (M_{is}). Comparisons are shown for the wing section located at $\approx 3.2\%$ of wingspan on the outboard side relative to the pylon trailing edge. Results are presented for cruise ($M_\infty = 0.85$), diversion ($M_\infty = 0.65$), and EOR ($M_\infty = 0.35$ and $M_\infty = 0.20$) in Figs. 15(a)-(d), respectively.

Figs. 15(a) and (b) show that predictions and measurements agree well in terms of the wing section M_{is} for both cruise and diversion conditions. The peak M_{is} is well predicted on both pressure and Suction Sides (SS) and the maximum difference between CFD analyses and measured data is of the order of 0.01 of ΔM_{is}. For the EOR cases when the 20-degree flap wing is used, Figs. 15(c) and (d) show that the flow topology is predicted to the same level of accuracy, except for the vicinity near the flap suction side where a consistent difference is noted between CFD and experimental measurements of the order of $\Delta M_{is} \approx 0.02$. This is due to a flow separation noted in the flap region. It is likely that this flow separation may be the root cause for the discrepancy between predictions and measurement of installed C_d^{Fan} suppression for $M_\infty = 0.35$ and for very low values of FNPR which reaches 2.2% (Fig. 5).

3.7. Estimation of installed engine mass flow at wind-milling

The measured and predicted C_d^{Fan} and C_d^{Core} performance maps were implemented into the developed 0D engine performance simulation model [35]. The goal was to estimate the impact of installed exhaust suppression on wind-milling engine air mass-flow and intake MFCR for EOR, diversion, and cruise conditions. The maps expressed C_d^{Fan} and C_d^{Core} as functions of M_∞, FNPR, and CNPR for each of the DSJP rig configurations (Fig. 2) in the form of tabulated nested data for the investigated conditions (Table 1). Therefore, the exhaust maps were localised around the analysed wind-milling conditions. Linear interpolation was used in the exhaust characteristics for all OD engine re-matching calculations. The handling parameter applied to achieve wind-milling flow through the engine was zero total enthalpy rise in the combustor.

Fig. 16 summarises the results of the 0D engine performance analyses. Results are presented in terms of percentage deltas of installed engine mass flow relative to the isolated case $\left(\frac{\dot{m}_{installed}^{engine} - \dot{m}_{isolated}^{engine}}{\dot{m}_{isolated}^{engine}}\right)(\%)$ across the range of flight M_∞ covering EOR, diversion, and cruise conditions. Results are presented for installed analyses using both the clean wing (blue markers) and the 20-degree flap wing (red markers). The circles correspond to analyses carried out using CFD derived performance maps for C_d^{Fan} and C_d^{Core}, whilst the triangles denote analyses performed using experimentally derived performance maps.

According to the analyses carried out using the experimental exhaust maps, the maximum engine air mass flow delta due to installed suppression is approximately -10%. This occurs when the high-lift surfaces are deployed (20-degree flap wing) at $M_\infty = 0.25$. This also changes the intake MFCR by about -10% relative to the isolated engine. This change in installed engine mass flow reduces to -4% at $M_\infty = 0.25$ when the clean-wing configuration is used. The impact of installed exhaust suppression on engine air mass-flow reduces to approximately -2.3% and -1.3% for

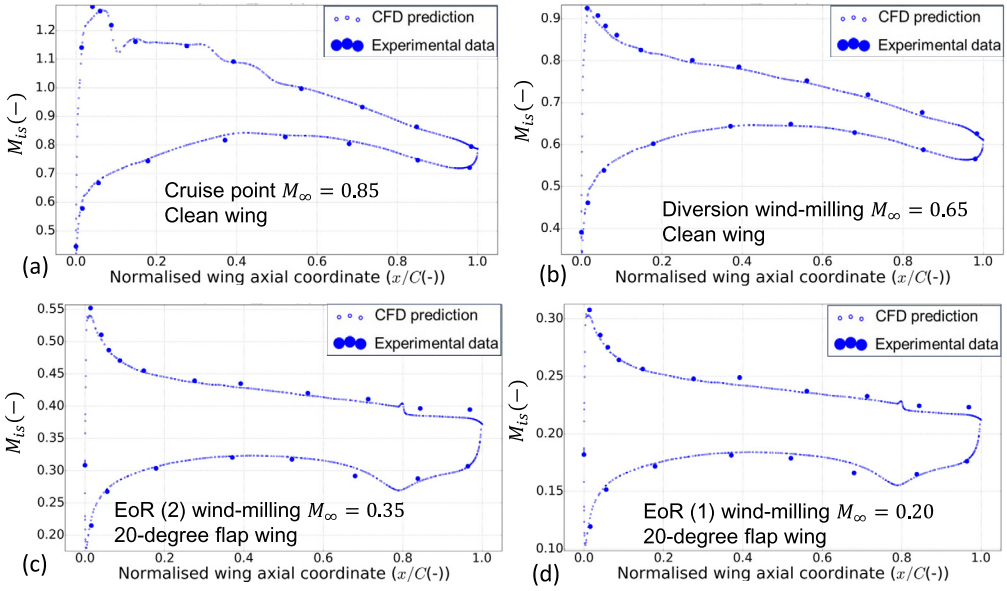


Fig. 15. Isentropic Mach number M_{is} on wing outboard side section (54 mm spanwise distance from pylon trailing edge – 3.2% of wingspan): (a) Cruise point $M_\infty = 0.85$, FNPR = 2.4, and CNPR = 1.71, (b) Wind-milling diversion $M_\infty = 0.65$, FNPR = 1.24, and CNPR = 1.08, (c) Wind-milling EOR (2) $M_\infty = 0.35$, FNPR = 1.05, and CNPR = 1.03 and (c) Wind-milling EOR (1) $M_\infty = 0.20$, FNPR = 1.03, and CNPR = 1.03.

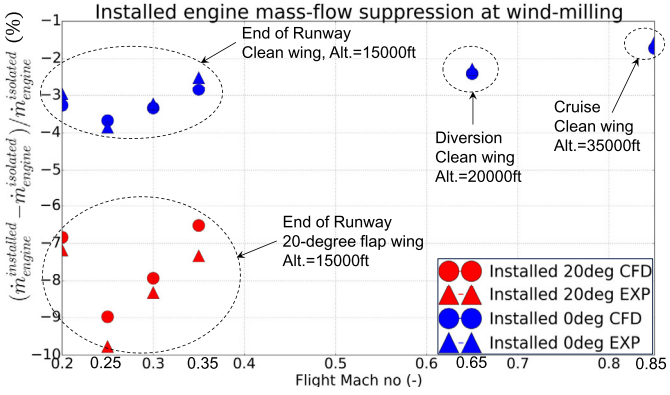


Fig. 16. Engine performance simulation: Impact of installed exhaust suppression on wind-milling engine mass flow relative to the isolated configuration $\left(\frac{\dot{m}^{engine}_{installed} - \dot{m}^{engine}_{isolated}}{\dot{m}^{engine}_{isolated}}\right)(\%)$.

the diversion ($M_\infty = 0.65$) and cruise ($M_\infty = 0.85$) conditions, respectively, where only the clean-wing configuration is used.

The analyses carried out using the CFD derived exhaust performance maps agree within 1% with the analyses performed using the measured data and the predicted maximum change in air mass flow due to suppression is roughly -9% for $M_\infty = 0.25$. The differences between analyses done using exhaust performance maps derived from measurements and CFD are consistently below 1% for all EOR cases with the 20-degree flap wing. This difference reduces to less than 0.5% for the clean wing at EOR conditions. This further reduces to roughly 0.25% for the diversion ($M_\infty = 0.65$) and cruise ($M_\infty = 0.85$) conditions. Therefore, CFD can produce credible global exhaust performance maps that extend to wind-milling conditions for sub-idle engine performance simulation.

Fig. 16 demonstrates that for the EOR cases ($M_\infty \in [0.20 - 0.35]$) the installed engine mass flow delta $\left(\frac{\dot{m}^{engine}_{installed} - \dot{m}^{engine}_{isolated}}{\dot{m}^{engine}_{isolated}}\right)(\%)$ exhibits a non-monotonic behaviour with M_∞. This is attributed to the opposing effects of M_∞ and FNPR on the installed fan nozzle suppression with increasing M_∞ [28]. Goulos et al. [28] showed that the installed C_d^{Fan} suppression effect reduces exponentially with increasing FNPR, whilst it increases quadratically with M_∞. When M_∞ increases, FNPR also increases due to the ram pressure rise and the two effects appear to oppose each other. The impact of M_∞ dominates until $M_\infty = 0.25$, whilst the favourable impact of an increasing FNPR appears to reduce the installed suppression effect for $M_\infty > 0.25$. This behaviour is observed for both the clean wing and the 20-degree flap wing (Fig. 16).

The impact of installation results in a small FNPR increase relative to the isolated configurations which reaches approximately 0.01 for $M_\infty = 0.35$ and for the 20-degree flap wing. This is due to the lower engine mass flow which reduces the Low-Pressure (LP) system loss [9] and concurrently increases the FNPR relative to the isolated system. This results in a reciprocal reduction of installed fan nozzle suppression [28] which increases the engine mass-flow. This process results in a non-linear effect which balances the implicit dependency between installed exhaust suppression, LP system loss, and wind-milling air mass-flow. This non-linear dependency is captured by the engine modelling approach which caters for the simultaneous resolution of all contributing physical mechanisms.

4. Conclusions

A combined experimental and numerical investigation was carried out to quantify the impact of installation on the aerodynamic behaviour of a civil large aero-engine exhaust at wind-milling. These included EOR take-off, diversion, and cruise wind-milling conditions for both isolated and installed configurations. The effects of FNPR, CNPR, M_∞, and high-lift surfaces on the installed exhaust suppression effect were quantified. The measured and predicted fan and core nozzle maps were implemented into a 0D engine performance model equipped with sub-idle component maps to quantify the changes in installed engine mass flow due to the impact of wing integration.

This work has quantified, for the first time, the effect of powerplant integration with a swept wing on exhaust suppression at off-design conditions. The effect of installation can reduce the fan and core nozzle discharge coefficients by up to 13% and 26%, respectively, relative to the isolated configuration for representative EOR wind-milling conditions. RANS CFD can capture the effect of installed suppression on both the fan and core with accuracy between 0.1% and 1.2%, depending on Mach number, which is sufficient for industrial design and analysis pur-

poses. The impact of the work is that it was shown for the first time that the installed suppression can reduce the installed engine mass flow by up to 10% for EOR wind-milling conditions. This effect has been omitted in engine airflow prediction methods found in the open literature which almost invariably assume that the fan and core nozzles exhaust to ambient static pressure at wind-milling [9,44]. This affects the intake $MFCR$ and must be taken into account for both engine performance modelling as well as the nacelle design [36,45].

The exhaust performance datasets reported in this work can be implemented into 0D modelling methods to improve the accuracy of sub-idle performance predictions for large aero-engines. This novel capability can be used to improve predictions of wind-milling LP system loss and fan operating conditions which are dependent on the fan nozzle discharge coefficient. Furthermore, the outcomes of this work enhance the design and analysis capabilities for aero-engine nacelles due to offering improved wind-milling $MFCR$ predictions. Therefore, the findings of this research directly improve the accuracy and robustness of aero-thermal modelling and nacelle design methods for future large aero-engines operating within the sub-idle wind-milling flow regime.

CRediT authorship contribution statement

Ioannis Goulos: Writing – review & editing, Writing – original draft, Visualization, Validation, Supervision, Software, Resources, Project administration, Methodology, Investigation, Funding acquisition, Formal analysis, Data curation, Conceptualization. **David MacManus:** Writing – review & editing, Supervision, Resources, Project administration, Methodology, Investigation, Funding acquisition, Conceptualization. **Josep Hueso Rebassa:** Writing – review & editing, Resources, Methodology, Formal analysis. **James Alderman:** Writing – review & editing, Validation, Supervision, Resources, Methodology, Investigation, Formal analysis, Data curation. **Christopher Sheaf:** Writing – review & editing, Supervision, Resources, Project administration, Investigation, Funding acquisition, Conceptualization.

Declaration of competing interest

The authors declare that they have no known competing financial interests or personal relationships that could have appeared to influence the work reported in this paper.

Acknowledgements

This project has received funding from the Clean Sky 2 Joint Undertaking (JU) under grant agreement number 101007598. The JU receives support from the European Union's Horizon 2020 research and innovation programme and the Clean Sky 2 JU members other than the Union.

Data availability

Due to commercial confidentiality agreements the supporting data is not available.

References

[1] F. Haselback, A. Newby, R. Parker, Next generation of large civil aircraft engines - concepts & technologies, in: European Turbomachinery Conference, Madrid, Spain, 23–27 March, 2015.
[2] A.H. Epstein, Aeropropulsion for commercial aviation in the twenty-first century and research directions needed, AIAA J. 52 (5) (May 2014) 901–911.
[3] N.T. Birch, 2020 vision: the prospects for large civil aircraft propulsion, Aeronaut. J. 104 (1038) (August 2000) 347–352.
[4] M. Waters, E. Schairer, Analysis of Turbofan Propulsion System Weight and Dimensions, NASA, TM X-73, Ames Research Center, Moffet Field, California, January 1977.
[5] D.L. Daggett, Ultra Efficient Engine Technology Systems Integration and Environmental Assessment, NASA, NASA/CR-2002-21175, Boeing Commercial Airplane Group, Seattle, Washington, 2002.
[6] A. Peters, Z.S. Spakovsky, W.K. Lord, B. Rose, Ultrashort nacelles for low fan pressure ratio propulsors, J. Turbomach. 137 (2) (February 2015), TURBO-14-1120.
[7] A. Swarthout, D. MacManus, J. Matensanz-Garcia, L. Boscagli, C. Sheaf, A comparative assessment of multiobjective optimisation methodologies for aero-engine nacelles, in: ICAS 33rd Technical Congress, ICAS 2022-0162, September 2022.
[8] N. Schreiner, F. Tejero, D. MacManus, C. Sheaf, Robust aerodynamic design of nacelles for future civil aero-engines, in: Proceedings of the ASME Turbo Expo 2020: Turbomachinery Technical Conference and Exposition, Volume 1: Aircraft Engine; Fans and Blowers, 1447, pp. 21–25, 2020.
[9] P.K. Zachos, Modelling and analysis of turbofan engines under windmilling conditions, J. Propuls. Power 29 (4) (July-August 2013) 882–890.
[10] N.G. Rosa, G. Dufour, R. Barenes, G. Lavergne, Experimental analysis of the global performance and the flow through a high-bypass turbofan in windmilling conditions, J. Turbomach. 137 (5) (May 2015), No. TURBO-14-1024.
[11] P. Walsh, P. Fletcher, Gas Turbine Performance, Blackwell Publishing, 2004.
[12] I. Goulos, J. Otter, F. Tejero, J.-H. Rebassa, D. MacManus, C. Sheaf, Civil turbofan propulsion aerodynamics: thrust-drag accounting and impact of engine installation position, Aerosp. Sci. Technol. 111 (106533) (April 2021).
[13] A.N. Rao, I. Goulos, D. MacManus, Impact of installation on a civil large turbofan exhaust system at idle descent conditions, Aerosp. Sci. Technol. 119 (107125) (2021).
[14] G. Subbian, A. Magrini, D. Buosi, R. Radespiel, R. Ponza, E. Benini, Investigation of HL-CRM aerodynamics with a UHBPR nacelle in powered-on condition, in: AIAA Propulsion and Energy Forum, AIAA 2021-3547, August 9-11, 2021.
[15] G. Subbian, A. Magrini, E. Benini, D. Buosi, R. Ponza, R. Radespiel, RANS analysis of HL-CRM at landing configuration with different flap deflections and engine representations, in: AIAA SciTech 2022 Forum, January 3-7, 2022.
[16] M. Robinson, D. MacManus, Aspects of aero-engine nacelle drag, Proc. Inst. Mech. Eng., G J. Aerosp. Eng. 233 (5) (May 2018) 1667–1682.
[17] I. Goulos, T. Stankowski, J. Otter, D. MacManus, N. Grech, C. Sheaf, Aerodynamic design of separate-jet exhausts for future civil aero-engine, Part 1: Parametric geometry definition and CFD approach, J. Eng. Gas Turbines Power 138 (8) (August 2016) 081201.
[18] I. Goulos, J. Otter, T. Stankowski, D. MacManus, N. Grech, C. Sheaf, Design optimisation of separate-jet exhausts for the next generation of civil aero-engines, Aeronaut. J. 122 (1256) (October 2018).
[19] J. Otter, I. Goulos, D. MacManus, M. Slaby, Aerodynamic analysis of civil aero-engine exhaust systems using computational fluid dynamics, J. Propuls. Power 34 (5) (September-October 2018) 1152–1165.
[20] G. Giangaspero, D. MacManus, I. Goulos, Surrogate models for the prediction of the aerodynamic performance of exhaust systems, Aerosp. Sci. Technol. 92 (9) (2019) 77–90.
[21] I. Goulos, J. Otter, T. Stankowski, D. MacManus, N. Grech, C. Sheaf, Aerodynamic design of separate-jet exhausts for future civil aero-engines, Part 2: Surrogate modeling and optimization, J. Eng. Gas Turbines Power 138 (8) (August 2016) 081202.
[22] J. Otter, T. Stankowski, M. Robinson, D. MacManus, Installation aerodynamics of civil aero-engine exhaust systems, Aerosp. Sci. Technol. 89 (June 2019).
[23] G.L. Oliveira, L.G. Trapp, A. Puppin-Macedo, Integration methodology for regional jet aircraft with underwing engines, in: 41st Aerospace Sciences Meeting and Exhibit, AIAA 2003-934, 6-9 January, Reno, Nevada, 2003.
[24] J.C. Vassberg, M.A. Dehaan, M.B. Rivers, R.A. Wahls, Development of a common research model for applied CFD validation studies, in: 26th AIAA Applied Aerodynamics Conference, No. AIAA Paper 2008-6919, 2008.
[25] A. Gomariz-Sancha, C. Sheaf, C.O.M. Gutierrez, Development of a dual stream jet propulsion rig for test and evaluation of engine nozzles in a transonic wind tunnel, AIAA SCITECH 2023 Forum, 23-27 January 2023, National Harbor, MD and Online, AIAA 2023-2009, https://doi.org/10.2514/6.2023-2009.
[26] K.L. Mikkelsen, D.J. Myren, D.G. Dahl, M.D. Christiansen, Initial subscale performance measurements of the AIAA dual separate flow reference (DSFR) nozzle, in: 51st AIAA/SAE/ASEE Joint Propulsion Conference, No. AIAA 2015-3883, Orlando, Florida, USA, 2015.
[27] D.I. Greenwell, Transonic industrial wind tunnels testing in the 2020s, Aeronaut. J. 126 (1295) (2022) 125–151.
[28] I. Goulos, J.H. Rebassa, F. Tejero, D. MacManus, A. Au, C. Sheaf, Impact of installation on the performance of an aero-engine exhaust at wind-milling flow conditions, J. Eng. Gas Turbines Power 145 (12) (December 2023).
[29] J.J. Otter, I. Goulos, R. Christie, D. MacManus, Design and analysis of non-axisymmetric installed aero-engine exhaust systems, Aerosp. Sci. Technol. 106 (November 2020) 106210.
[30] E.J. Gunn, C.A. Hall, Loss and deviation in windmilling fans, J. Turbomach. 138 (10) (4 2016).
[31] L.E. Ferrer-Vidal, A. Iglesias-Perez, V. Pachidis, Characterization of axial compressor performance at locked rotor and torque-free windmill conditions, Aerosp. Sci. Technol. 101 (June 2020) 105846.
[32] L.E. Ferrer-Vidal, V. Pachidis, R.J. Tunstall, Generating axial compressor maps to zero speed, Proc. Inst. Mech. Eng. A, J. Power Energy 235 (2021) 956–973.
[33] L.E. Ferrer-Vidal, V. Pachidis, Numerical modeling of core compressor discharge for a windmilling aero engine, Aerosp. Sci. Technol. 108 (June 2021) 106365.
[34] ANSYS, ANSYS Fluent User's Guide. Release 19.1, Canonsburg, PA, USA, 2019.
[35] J.K. Lythle, The numerical propulsion system simulation: an overview, in: National Aeronautics and Space Administration, TM-2000-209915, Glen Research Centre, Cleveland, Ohio, 2000.

[36] A. Swarthout, D. MacManus, F. Tejero, J. Matesanz-Garcia, I. Goulos, L. Boscagli, Aerodynamics of a compact nacelle at take-off conditions, in: AIAA Aviation Forum 2023, San Diego, CA, June 2023, pp. 12–16, No. 10.2514/6.2023-3309.

[37] European Committee for Standardization, BS EN ISO 9300:2005, Measurement of gas flow by means of critical flow Venturi nozzles, August 2005.

[38] C.B. Robert, G. Casella, Monte Carlo Statistical Methods, Springer, New York, ISBN 978-0-387-21239-5.

[39] W.H. Press, S.A. Teukolsky, W.T. Vetterling, B. Flanerry, Numerical Recipes 3rd Edition: The Art of Scientific Computing, Cambridge University Press, Cambridge, England, 2007.

[40] Ansys Inc, 275 Technology Drive, Canonsburg, PA 15317, ANSYS WORKBENCH User's Guide.

[41] ANSYS, I., ANSYS FLUENT Theory Guide: Release 16.2, ANSYS, Canonsburg, PA, 2013.

[42] F. Menter, Two-equation eddy-viscosity turbulence models for engineering applications, AIAA J. 32 (8) (August 1994) 1598–1605.

[43] W. Sutherland, The viscosity of gases and molecular forces, Philos. Mag. 36 (1893) 507–531.

[44] ESDU, Estimation of Windmilling Drag and Airflow of Turbo-Jet and Turbo-Fan Engines, Tech. Rep., ESDU-81009, 2000.

[45] ESDU, Estimation of Spillage Drag for a Wide Range of Axisymmetric Intakes at M Less than 1, Tech. Rep., ESDU 84004, 2000.



https://dspace.org/

Impact of installation on the performance of a civil turbofan exhaust at wind-milling: a combined experimental and numerical approach

Goulos, Ioannis; MacManus, David G.; Hueso Rebassa, Josep; Alderman, James; Sheaf, Christopher T.

2025-03
Elsevier
https://doi.org/10.1016/j.ast.2024.109883
Goulos I, MacManus D, Hueso Rebassa J, et al., (2025) Impact of installation on the performance of a civil turbofan exhaust at wind-milling: a combined experimental and numerical approach. Aerospace Science and Technology, Volume 158, March 2025, Article number 109883

Downloaded from a DSpace repository. https://dspace.org/